Materials Today Chemistry 56 (2026) 104002

Contents lists available at ScienceDirect

Materials Today Chemistry

journal homepage: www.journals.elsevier.com/materials-today-chemistry/

# Robust water-based synthesis of monodisperse ultrasmall SPIONs with tunable $T_1$-$T_2$ relaxometric behaviour as MRI contrast agents

Daniela Meroni [a,b], Davide Cicolari [c,d], Giorgia Colciago [e], Tommaso Taroni [a], Laura Rossi [f], Marco Maria Jacopo Felisi [c], Paola Enrica Colombo [c], Francesco Orsini [b,d], Riccardo Vago [e,g], Daniela Maggioni [a,b,*], Paolo Arosio [b,d]

[a] Department of Chemistry, Università degli Studi di Milano, Via Golgi, 19, Milano, 20133, Italy
[b] Consorzio INSTM, Via Giusti, 9, Florence, 50121, Italy
[c] Department of Medical Physics, ASST Grande Ospedale Metropolitano Niguarda, Milano, Italy
[d] Department of Physics, Università degli Studi di Milano, Via Celoria, 16, Milano, 20133, Italy
[e] Urological Research Institute, Division of Experimental Oncology, IRCCS San Raffaele Scientific Institute, Via Olgettina, 60, Milano, 20132, Italy
[f] Chemical Engineering Department, TUDelft, the Netherlands
[g] Università Vita-Salute San Raffaele, Via Olgettina, 58, Milano, 20132, Italy

ARTICLE INFO

*Keywords:*
Ultrasmall magnetic nanoparticles
Coprecipitation
Relaxivity
MRI
Contrast agent

ABSTRACT

Magnetite-based nanoparticles (MNPs) are widely investigated for biomedical applications including hyperthermia, drug delivery and magnetic resonance imaging (MRI). Precise control of their morphology is essential and typically achieved via thermal decomposition, though more scalable and energy-efficient approaches are needed, especially for ultrasmall (<5 nm) MNPs. Here, well-controlled MNPs were synthesized by optimizing a coprecipitation process conducted at low temperature and in air, without polymeric stabilizers or templates. The combined use of tetramethylammonium hydroxide (TMAOH) as a base, citric acid to quench growth, and controlled reaction temperature (from room temperature to 0 °C), enabled the reproducible formation of monodisperse, highly crystalline MNPs with core size tunable from 6.6 to 4.0 nm, as confirmed by (HR)TEM. The TMAOH could be readily replaced by citrate as biocompatible stabilizer, forming a 1 nm-thick shell (AFM) and ensuring long-term stability, even under magnetic fields. NMRD measurements (0.01-57 MHz) showed superparamagnetic behaviour and a size-dependent transition from $T_2$-to $T_1$-type relaxation, with $r_2/r_1$ ratio at 1.34 T decreasing from 3.3, 2.9, and 1.8 for 6.6, 5.3, and 4.0 nm particles, respectively. MRI at 3 T confirmed that the smaller MNPs exhibit significant $T_1$ contrast. Finally, MNP@citrate were stable in cell culture medium, well tolerated at all tested concentrations ($C_{max}$ = 140 μg/mL) on Human Embryonic Kidney 293 (HEK) cells, and accumulated in the cytoplasm within 24 h incubation, as shown by reflectance confocal microscopy.

## 1. Introduction

Magnetic Resonance Imaging (MRI) is a non-invasive imaging technique widely used for clinical diagnosis and biomedical research, offering excellent spatial resolution and soft tissue contrast without the use of ionizing radiation. The diagnostic efficacy of MRI is greatly enhanced by contrast agents (CAs), which improve image contrast by locally shortening the longitudinal, $T_1$, and/or transverse, $T_2$, nuclear relaxation times of tissues. Gadolinium-based contrast agents, CAs used in clinical practice, primarily shorten the $T_1$ time, producing a marked positive contrast in $T_1$-weighted images [1]. However, Gd-based CAs have been associated with a number of serious health concerns, including nephrogenic systemic fibrosis in patients with impaired renal function and long-term accumulation of gadolinium in tissues such as the brain, bones, and skin [2,3]. These safety issues have led to increasing regulatory scrutiny and have motivated the search for safer alternatives.

Superparamagnetic iron oxide nanoparticles (SPIONs) have emerged as promising candidates to replace Gd-based CAs in certain circumstances due to their biocompatibility, metabolic clearance through endogenous iron pathways, and strong magnetic responsiveness [4]. Owing to these properties, SPIONs have found several biomedical

* Corresponding author. Department of Chemistry, Università degli Studi di Milano, Italy.
*E-mail address:* daniela.maggioni@unimi.it (D. Maggioni).

https://doi.org/10.1016/j.mtchem.2026.104002
Received 4 June 2026; Received in revised form 6 August 2026; Accepted 29 August 2026

applications including theranostics [5], magnetic scaffolds for regenerative medicine procedures [6], magnetophoresis [7,8], cancer cell destruction via hyperthermia [9,10] and magneto-mechanical effects [11]. Nonetheless, traditional SPIONs are relatively large and act predominantly as $T_2$ contrast agents, inducing a negative contrast in $T_2$-weighted images [12–16]. This type of contrast can be less desirable for certain clinical applications due to lower specificity and potential for diagnostic ambiguity [17]. Despite the commercial availability of SPION-based $T_2$ agents such as Resovist and Feridex, these products were scarcely used and eventually withdrawn from the market due to limited clinical uptake and competition from $T_1$ agents.

More recently, attention has shifted to ultrasmall SPIONs (USPIONs), typically defined as iron oxide nanoparticles with core diameters below ~5 nm [18,19]. At this size scale, the particles exhibit reduced magnetic susceptibility and faster proton exchange rates, which favour $T_1$ relaxation mechanisms and result in positive contrast in MRI $T_1$-weighted scans. USPIONs thus combine the favourable safety profile of SPIONs with the imaging characteristics of Gd-based CAs. Moreover, it has been reported that MRI dual-activatable $T_2$-$T_1$ and $T_1$-$T_2$ contrast agents can be obtained resulting in high sensitivity detection of tumour lesions [20,21].

Several synthetic routes have been explored for producing USPIONs, including thermal decomposition, reduction of iron salts, solvothermal methods, and co-precipitation [22]. Among these, the thermal decomposition approach provides excellent control over size and crystallinity but suffers from high costs of reagents and equipment, use of organic solvents, complex procedures, and limited scalability, making it less attractive for clinical translation [22]. In contrast, the co-precipitation method is attractive for its simplicity, low cost, aqueous environment, and scalability [23]. It has the lowest synthetic requirements, as it can be carried out at or near room temperature and environmental conditions, in aqueous solvent and using low-cost and benign reagents, with the least amount of time. This approach involves the stoichiometric reaction of Fe(II) and Fe(III) salts with a base (commonly NaOH or $NH_4OH$) in water to form magnetite ($Fe_3O_4$) nanoparticles according to the reaction:

$$Fe^{2+} + 2Fe^{3+} + 8OH^- \rightarrow Fe_3O_4 + 4H_2O \quad \text{(eq. 1)}$$

Recently, some authors have demonstrated the compatibility of this synthetic approach with flow synthesis [24]. However, the standard co-precipitation technique presents major limitations when aiming to synthesize USPIONs. The process typically yields larger, polydisperse nanoparticles due to rapid poorly controlled nucleation and growth steps. In particular, the choice of the base plays a critical role: recent studies [24] have shown that the use of sodium hydroxide leads to uncontrolled nucleation and larger particle sizes, making it unsuitable for producing ultrasmall, monodisperse SPIONs. Alternative strategies, such as the use of more sophisticated chelating agents, surfactants [25,26] or homogeneous and rapid cooling of the reaction mixture to quench the growth, can improve size control [27]. However, these approaches also complicate the synthesis and may compromise its scalability and environmental compatibility.

In this work, we report a new and robust co-precipitation protocol for the synthesis of ultrasmall SPIONs characterized by high monodispersity, colloidal stability in aqueous suspension, and favourable magnetic properties for $T_1$-$T_2$ dual mode MRI applications, which have been studied by relaxometric measurements at different resonance frequencies (NMRD) [16,28], as well as by MRI. The synthesis of USPIONs is achieved with a simple approach without the use of surfactants, complex chelating agents or sophisticated equipment, thereby overcoming a major obstacle in the translation of USPIONs as $T_1$-contrast agent for commercial applications.

## 2. Experimental part

### 2.1. Reagents

$FeCl_2{\cdot}4H_2O$ (J.T. Baker), $FeCl_3 \bullet 6H_2O$ (Merck), NaOH (32%, Fluka), HCl (30%, Suprapur, Merck), tetramethylammonium hydroxide (25% w/w, Merck; *Caution! TMAOH is highly hazardous and toxic. It is a strong, corrosive alkali that is acutely toxic if inhaled, swallowed, or absorbed through the skin. Handle it under a fume hood while wearing all the appropriate personal protective equipment*), hydroxylamine hydrochloride (ABCR), glacial acetic acid (Merck), Mohr salt (Merck), phenanthroline monohydrate (ABCR) were used as received. Ultrapure water (Milli-Q, Millipore, resistivity 18 MΩ $cm^{-2}$) was employed for the preparation of all the solutions.

### 2.2. Synthesis of MNP

For the MNP syntheses, a 0.5 M aqueous stock solution of Fe(III) was prepared by dissolving the proper amount of $FeCl_3{\cdot}6H_2O$ in water. In a typical synthesis, in a 20 mL vial, 250 μL of 0.5 M $FeCl_3$ stock solution were poured in 7.2 mL water. Then, 0.178 g of $FeSO_4 \bullet 7H_2O$ were dissolved in 2 mL water, resulting in a 0.320 M solution, and immediately after the dissolution of the Fe(II) salt (30-60 s), 200 μL were added to the diluted Fe(III) salt solution under vigorous magnetic stirring. Hence, 300 μL of 25% w/w TMAOH were added in one shot, and a sudden colour change from clear pale yellow to black occurred, indicating the onset of nanoparticle nucleation, which in this reaction occurs very quickly even at room temperature. The solution was left under stirring for 1 or 5 min (growth time). If the reacting temperature was different from room temperature, the salt mixture was cooled to 0 °C, and only after the TMAOH was added and the mixture maintained at low temperature also for the growth time. Afterwards, 50 μL of a 3.2 M citric acid solution was added, and the magnetic stirring was continued for another 20 min. The magnetic stir bar was then quickly removed, to prevent it from acting as an aggregation centre for magnetic nanoparticles.

The purification of the MNP were carried out either by dialysis (12-14 kDa cutoff, 72 h) or by ultrafiltration by centrifugation employing an Eppendorf 5430 centrifuge equipped with a F-35-6-30 fixed-angle rotor, using Amicon Ultra-15 centrifugal filter devices (Millipore) with 3000 nominal molecular weight limit (NMWL) RC membranes. The MNP suspensions were diluted 1:5 with water and centrifugations (5000 rpm, 25 min) were repeated until the FTIR spectra of retained MNP no longer showed the TMAOH bands. To stabilize the MNP, an addition of trisodium citrate aqueous solution (113 μL, 1.33 M) was performed.

### 2.3. Instruments and Methods

*DLS* and *ζ-potential* measurements were carried out on as synthesized MNPs, as well as after purification and after citrate addition, monitoring their properties over time. Additionally, tests were also carried out by dispersing the MNPs in cell culture medium (as described in Section 2.4). Analyses were performed on a Zetasizer Nano ZS instrument (Malvern Instruments Corp.) equipped with a solid state He-Ne laser emitting at a wavelength of 633 nm and collecting the scattered light at a scattering angle of 173°, at 298 K on diluted samples. Each hydrodynamic diameter was averaged from at least three measurements. Standard deviations of the diffusion coefficients were obtained as the half of the full width at half maximum (FWHM) of the size distribution by intensity peaks as derived by the Malvern software.

*ATR-FTIR* spectra were acquired on a PerkinElmer Frontier instrument equipped with an ATR accessory with a diamond/ZnSe crystal, recording the IR spectra in the wavenumber range between 4000 and 400 $cm^{-1}$.

*Transmission Electron Microscopy* (TEM) experiments were carried out using either a FEI Tecnai F20 Field Emission Gun electron microscope with a 100 kV accelerating voltage or a HRTEM Zeiss Libra 200FE

electron microscope with a 200 kV accelerating voltage. The samples were first diluted in water and sonicated for a few minutes. A drop was then placed onto a 300-mesh carbon-coated copper grid and left dry for 15 min by using an infrared lamp before the analysis. Alternatively, the copper grid was dip coated by immersing it for a few seconds in the diluted suspensions of MNP and then left drying overnight in air at room temperature before the analysis.

pH *measurements* were carried out using an AMEL 338 pH-meter equipped with a 411/CGG/6 combined electrode from AMEL.

Iron concentration was determined by *ICP-OES analysis* on a PerkinElmer Optima 8300 instrument. The proper amount of suspension, depending on the analyzed sample (30-150 μL), were added with 200 μL HCl 37% w/w and left digesting overnight in a 10 mL flask. Then, the yellowish and clear solution was brought to volume by adding water. Iron concentration was also determined by a well-known spectrophotometric method adopting the internal standard method [29]. A 0.72 mM Fe(II) standard solution was prepared dissolving the Mohr salt (28.0 mg) in a 100 mL flask with water. For each MNP sample, four 10 mL flasks were prepared adding 0, 0.5, 1 and 1.5 ppm of Fe(II) from the standard solution. Prior to sample preparation, the flasks were treated with aqua regia and thoroughly rinsed with water. Then, the proper amount of MNP suspension was digested with 750 μL HCl 37% and, after 1 h at room temperature, 100 μL $NH_2OH$ 10% w/w were added to quantitatively reduce all the Fe(III) to Fe(II). After a few minutes, 6 mL of acetate buffer (5 M, pH 4.93) were added to keep pH to 5-6. Then, 200 μL of a 0.03 M 1,10-phenanthroline hydro-alcoholic solution turned the colour from uncoloured to pink-orange. Finally, the flasks were brought to volume with Milli-Q water. For each solution, a UV-vis spectrum was acquired monitoring the absorbance variation at 512 nm. UV−vis absorption spectra were acquired on a UV-2600 Shimadzu spectrophotometer at room temperature.

*AFM imaging* was performed using a Nanoscope Multimode IIId system (Bruker) operating in tapping mode in air at room temperature. AFM images were obtained using the RMS amplitude of the cantilever as the feedback signal for the vertical sample position. The RMS free amplitude of the cantilever was approximately 15 nm and the relative set-point was above 95% of the free amplitude. Rectangular silicon nitride probes with a nominal spring constant of ~2.5 N $m^{-1}$ (NT-MDT) and cantilever length of 20 μm were used. The cantilever resonance frequency was about 130 kHz. The mica support (Ted Pella) was glued to a metal disk that was magnetically fixed to the AFM sample holder. The images were recorded at a line rate of ~1 Hz, and a resolution of 512 × 512 pixels per image was chosen. All AFM images were subjected to a line-by-line subtraction of the linear background to eliminate sample tilt from the images and correct for stepwise changes between individual scan lines. The size of the MNPs, evaluated from the AFM data, was reported in the work as the mean value ± the standard deviation calculated considering n = 25 single MNPs visualized in several AFM topography images.

*Nuclear magnetic resonance (NMR) and relaxivity.* The longitudinal, $T_1$, and transverse, $T_2$, nuclear relaxation times were acquired over a wide range of Larmor frequencies ($0.01 < \nu < 57$ MHz), i.e., external static magnetic fields of $\mu_0 H = 0.00023 - 1.34$ T ($\nu = \gamma(\mu_0 H)/2\pi$, where $\nu$ is the Larmor frequency and $\gamma/2\pi = 42.58$ MHz $T^{-1}$). The relaxivity, i.e. the efficiency of MNPs as a CA, was evaluated at each frequency. The magnetic field range was chosen to cover the most typical fields used in clinical and research laboratory MRI tomography ($\mu_0 H = 0.2$, 0.5, and 1.5 T). Different instrumentation and acquisition sequences were used depending on the frequency range:

- 0.01MHz $< \nu <$ 7.2MHz. The fast field cycling technique was performed using a fast-field-cycling NMR SMARTracer relaxometer (Stelar s.r.l.) [30]. In the case of measurements using $\nu < 4$ MHz, pre-polarized (PP) pulse sequences were applied to overcome the low signal-to-noise ratio: saturation recovery (SR) for $T_1$ and spin-echo (SE) for $T_2$. For $\nu > 3.7$ MHz, no pre-polarization procedure was applied, and thus no pre-polarized (NP) pulse sequences were used. For $T_1$ and $T_2$ measurements, the standard SR sequence and a classical Carr–Purcell–Meiboom–Gill (CPMG) sequence were applied, respectively.
- 7.2MHz $< \nu <$ 57MHz. The acquisitions were performed using a Stelar Spinmaster Fourier transform nuclear magnetic resonance spectrometer with standard SR pulse sequence to acquire $T_1$, while CPMG was used for $T_2$ acquisitions.

All measurements were conducted at room temperature. The NMR samples were prepared by diluting the MNP dispersions in ultrapure water to achieve a millimolar concentration. From the $T_1$ and $T_2$ measurements, the longitudinal (i = 1) and transverse (i = 2) nuclear relaxivities, $r_i$, are calculated by means of:

$$r_i = \frac{1}{C} \cdot \left( \frac{1}{T_{i,m}} - \frac{1}{T_{i,dia}} \right) \quad i = 1, 2 \qquad \text{(eq. 2)}$$

where $C$ is the concentration of the magnetic centres (millimolar, mM), $T_{i,m}$ is the relaxation time of hydrogen nuclei in the presence of contrast agents (i.e. MNP), and $T_{i,dia}$ is the relaxation time of the hydrogen nuclei in the dispersant medium (diamagnetic, dia). From the relaxivity values as a function of investigated frequency, we obtained the NMR Dispersion (NMRD) profiles for each sample, where the error on the relaxivity values was calculated a priori to be ~8%, due to the electronics and the error on the acquisition parameters.

*MRI.* $T_1$- and $T_2$-weighted images were acquired using a 3 T Siemens Vida MRI scanner with a 16-channels Head-Neck paediatric coil and standard 2D spin-echo sequences at room temperature. Hereafter are listed the acquisition parameters: (i) $T_1$-weighted: $T_R/T_E$ = 500/12 ms, Flip Angle = 90°, Number of Average = 3, Slice thickness = 5 mm, Field of View = 150 mm, Acquisition matrix = 256x256, Reconstruction matrix = 512x512, Imaging frequency = 123.22 MHz. (ii) $T_2$-weighted: $T_R/T_E$ = 5000/200 ms, Flip Angle = 90°, Number of Average = 1, Slice thickness = 5 mm, Field of View = 150 mm, Acquisition matrix = 256x256, Reconstruction matrix = 512x512, Imaging frequency = 123.22 MHz.

### 2.4. Cell cultures

Human Embryonic Kidney (HEK) cells were cultured in Dulbecco's Modified Eagle Medium (Gibco, Life Technologies Corporation), supplemented with 10% fetal bovine serum (Euroclone), 1% of penicillin/streptomycin (Gibco, Life Technologies Corporation). Cells were maintained at 37 °C in a humidified atmosphere of 5% $CO_2$.

### 2.5. Cell viability assay

HEK cells ($5 \times 10^3$ cells/well) were seeded in 96 wells plates and incubated with 140, 70, 30, 10 e 3 μg/mL MNP, in addition to a blank containing only the equivalent citrate solution. Before their use, MNP suspension was centrifuged (15000 g, 10 min, 1x), and the collected pellet was easily redispersed in a 0.01 M citrate solution. After 72 h at 37 °C, cell viability was evaluated with a previously reported procedure [31]. Briefly, 3-(4,5-dimethylthiazol-2-yl)-2,5-diphenyltetrazolium bromide (MTT, Sigma-Aldrich) (5 mg/mL in PBS) was added (0.5 mg/mL working concentration). After 1 h incubation at 37 °C, the supernatants were removed, and 100 μL/well of dimethyl sulfoxide was added to dissolve the formazan crystals. Cell viability was assessed by measuring the absorbance at 570 nm and expressed as a percentage of the untreated control. Data were shown as the mean ± SD from three independent experiments performed in quadruplicate.

### 2.6. Immunofluorescence analysis

HEK cells were seeded in sub-confluent conditions and grown

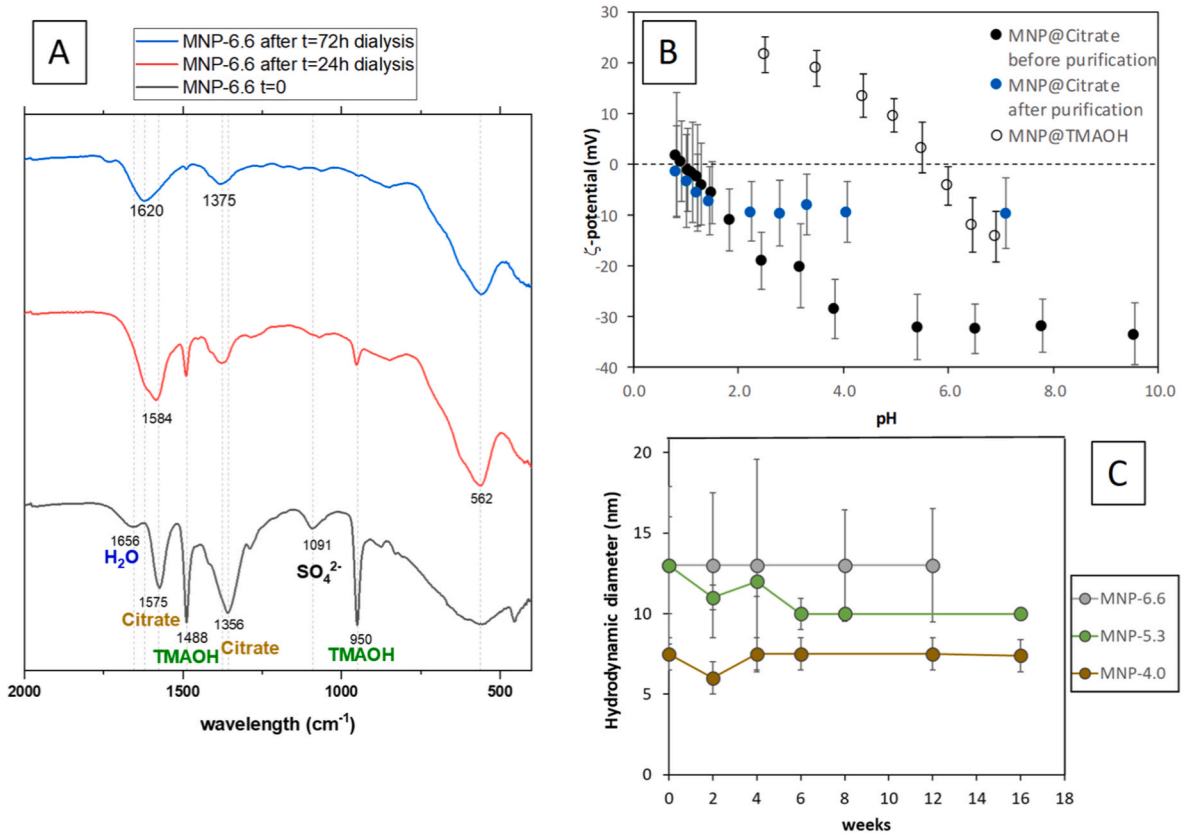


**Fig. 1.** A) ATR-FTIR spectra before and after 24 and 72 h dialysis. **B)** ζ-potential as a function of pH for MNPs synthesized with and without citrate addition, before and after purification. **C)** Hydrodynamic diameter by DLS (intensities) for three different samples obtained in this work (see below), purified by dialysis and added with trisodium citrate (final pH = 7.4).

overnight on glass coverslips. They were incubated with 70 μg/mL MNP for both 4 and 24 h, washed with PBS and fixed in 4% paraformaldehyde in PBS at room temperature for 10 min. After extensive PBS washing to remove the excess of paraformaldehyde, cells were incubated 30 min at room temperature in a dark chamber with Alexa Fluor 488 Phalloidin 1:40 (Gibco, Life Technologies Corporation, Cat n°A12379) and Hoechst 33342 Trihydrochloride, Trihydrate 1:1000 (Gibco, Life Technologies Corporation, Cat. n°H1399) in 0.1% donkey serum, 0.1% Triton in PBS. Coverslips with stained cells were mounted on a microscope slide with Fluorescent mounting medium (Dako North America, Inc. Cat n°S3023). Reflection and fluorescent images were acquired using a Nikon A1 laser scanning confocal microscope (CLSM) with a 60x oil immersion objective (NA 1.4). Images were acquired exciting the samples using a 405 nm laser line for the nuclei and a 488 nm laser line for the actin filaments, collecting the emitted signals using a 450/50 and a 525/50 emission filter, respectively. Nanoparticle aggregates were observed in reflection mode. Images were processed with ImageJ software.

## 3. Results and discussion

### 3.1. Synthesis and purification of USPION@citrate

The synthesis of magnetite USPIONs was achieved by a very simple but robust and reproducible coprecipitation method, which employs $FeCl_3$ and $FeSO_4$ in strictly stoichiometric amounts (2:1, respectively) and the base tetramethylammonium hydroxide (TMAOH). The formation of magnetite nanoparticles via coprecipitation synthesis, when conducted with an abrupt pH increase, occurs rapidly, as indicated by the immediate colour change following base addition. According to the LaMer model, after this sudden pH rise, iron hydroxides and aquo-hydroxo complexes are formed, including intermediates such as $[Fe_2(OH)_4(H_2O)_8]$ and $[Fe_2(OH)_6(H_2O)_6]$ [32]. Once these precursors reach saturation, a burst nucleation occurs, initially forming tiny ferrihydrite nanoparticles, which subsequently develop into magnetite nanoparticles [33]. The formed nuclei are rich in coordinatively unsaturated iron centres as well as oxygen atoms on their surface, which are thought to be quickly passivated by $OH^-$ and $H_2O$ molecules, creating a high energy barrier toward further growth [34]. However, due to the very low solubility of magnetite in basic environment, a precipitate instantly forms when alkaline agents such as $NH_4OH$ and NaOH are employed. Here, TMAOH was quickly added under strong magnetic stirring. Unlike more commonly employed alkaline agents, our results show that stable colloidal suspensions of iron oxide nanoparticles are formed when TMAOH is used as base (Fig. S1) without producing any precipitate observable to the naked eye. It has been previously reported that USPIONs (core diameter < 5 nm) could not be obtained when NaOH was used as the base in the coprecipitation process [35]. The displayed colloidal stability can be traced back to the adsorption of $[N(CH_3)_4]^+$ at the surface of the negatively charged nanoparticles at a certain extent (see below). TMAOH has been earlier reported to act as peptizing agent for the re-dispersion of the magnetic precipitate obtained in conventional coprecipitation syntheses after the increase of the pH [36,37]. It should be noted that, to the best of our knowledge, no previous literature reports have described the use of TMAOH as a base for the synthesis of USPIONs.

After a growth time of 1-5 min, a citric acid solution is added to the suspension to quench the nanoparticle growth by decreasing the pH from alkaline to mild acidic conditions. Moreover, before citric acid addition, considerable aggregation is appreciable (Fig. S2): adsorption of citrate ions at the surface promotes disaggregation, which is complete within 24 h. The amount of citric acid was optimized by preparing four identical MNP samples differing only in the volume of citric acid added

**Table 1**
DLS size distribution by intensity before purification for the main peaks of samples synthesized varying the TMAOH: Fe(III) molar ratio (RT, 156 mM $Fe^{3+}$, 5 min of growth): average hydrodynamic diameters, $\overline{D}_h$ (standard deviation reported in parentheses), and size distribution (as half peak width at half-maximum, $\sigma_D$).

| TMAOH/Fe(III) molar ratio | $\overline{D}_h$ (nm) | $\sigma_D$ (nm) | $\overline{D}_h$ (nm) | $\sigma_D$ (nm) |
|---|---|---|---|---|
| > 8 | 33 (8) | 5 | 139 (3) | 44 |
| 7 | 37 (13) | 8 | 121 (23) | 40 |
| 4.8 | 17.5 (3) | 7 | 91 (7) | 42 |
| 4.2 | 14 (2) | 6 | 75 (10) | 40 |

**Table 2**
Average hydrodynamic diameters ($\overline{D}_h$) of the main DLS peak (by intensities) for purified samples synthesized varying the initial iron concentration, growth time and reaction temperature. Standard deviation values are reported in parenthesis. Size distributions, as half of the full width at half maximum ($\sigma_D$), are also reported.

| Temperature | growth time (min) | $[Fe^{3+}]_0$ = 156 mM | | $[Fe^{3+}]_0$ = 15.6 mM | |
|---|---|---|---|---|---|
| | | $\overline{D}_h$ (nm) | $\sigma_D$ (nm) | $\overline{D}_h$ (nm) | $\sigma_D$ (nm) |
| RT | 5 | 15(2) | 6 | 15(3) | 7 |
| | 1 | 24(1) | 12 | 12(1) | 5 |
| 0 °C | 5 | 13(1) | 5 | 13(1) | 5 |
| | 1 | 13(1) | 4 | 7(1) | 2 |

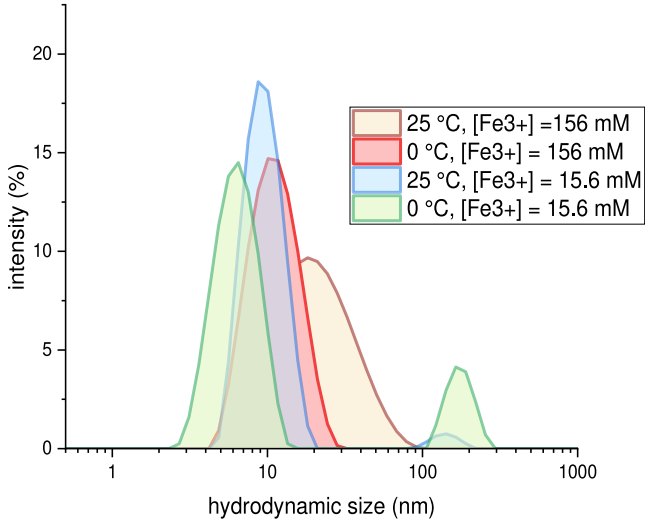


**Fig. 2.** Comparison of DLS size distribution by intensity of samples synthesized at different temperatures (25 and 0 °C) and concentrations (156 and 15.6 mM), all other parameters equal ([TMAOH]/$[Fe^{3+}]$ = 4.8, growth time 1 min). Sample synthesized at 60 °C is not reported as it immediately formed a precipitate.

at the end of the growth step. Table S1 shows that the largest tested amount of citric acid led to a low pH value measured immediately after the synthesis, resulting in fast disaggregation of the formed MNPs, but also in their dissolution within few days, as indicated by change in colour of the suspension from dark brown to clear yellow. Conversely, the lowest tested amount of citric acid proved insufficient at disaggregating the MNPs, as suggested by DLS showing persistent aggregation even after one week. Among the tested amounts, we selected the condition providing both the smallest hydrodynamic size and the best colloidal stability (50 μL). These findings agree with the literature studies showing that citric acid influences not only the aggregation state of MNPs from coprecipitation synthesis but also the final particle size [24,26,38].

The variation of several parameters, such as the mode, rate, and sequence of addition, did not show any significant effect on the outcome of the synthesis. Furthermore, each synthesis was carried out by different operators over several years, using different batches and brands of reagents and in different laboratories, consistently demonstrating high reproducibility of the results. This highlights the remarkable robustness of the method, likely attributable both to its operational simplicity and to the peptizing and basifying action of TMAOH, which helps overcome one of the main limitations of coprecipitation-based syntheses.

However, TMAOH is known to have both corrosive properties and systemic toxicity due to the $TMA^+$ cation [39]. For this reason, in our synthetic protocol, TMAOH is used as a base during initial stages of nanoparticle synthesis and it is not intended to be present in the final formulation. To this end, the toxic TMAOH was replaced by a post synthetic ligand exchange with citrate, which was selected due to its high biocompatibility and the ability to enhance electrostatic repulsion between nanoparticles, thus preventing aggregation over a wide range of pH at low to moderate ionic strength.

The TMAOH as well as the exceeding citrate are removed by either dialysis (Fig. 1a) or ultrafiltration by centrifugation (Fig. S2) monitoring the purification procedure by ATR-FTIR. Fig. 1a shows, as a representative example, the ATR-FTIR spectra of the MNP sample of average size of 6 nm, before and after dialysis using a membrane with a 12-14 kDa cut-off. The characteristic sharp TMAOH bands, attributed to the C-H asymmetric bending (1488 $cm^{-1}$) and the C-N asymmetric stretching (950 $cm^{-1}$), are considerably reduced after 3-day dialysis. Also the band at 1091 $cm^{-1}$, attributed to the sulphate anions, completely disappear at the end of the dialysis process, while the citrate bands at 1575 and 1356 $cm^{-1}$ (asymmetric and symmetric stretching of the carboxyl group, respectively) broaden and shift to the final values of 1620 and 1375 $cm^{-1}$ ($\Delta\nu = \nu_{asymm} - \nu_{symm}$ = 245 $cm^{-1}$), probably due to the elimination of the citrate excess not interacting with the nanoparticles during the purification. Previous works have consistently reported $\Delta\nu$ ~236–246 $cm^{-1}$ [40], which have been related to monodentate-type coordination between the carboxylate and the oxide surface [41]. After 1 day of dialysis, upon removal of overlapping bands related to the synthesis residues, the band of the magnetite lattice at 562 $cm^{-1}$ clearly emerged. It can also be noted that this band remains predominant even after purification, which is carried out under air, i.e. in oxidizing conditions. The shape of this broad band remained unchanged for several days, even when the sample was stored under ambient conditions. An enrichment in the maghemite phase can be suggested, based on the appearance of a band at ca 630 cm-1 [42], only after several weeks of storage under air, in agreement with the slow conversion rate of

**Table 3**
Reaction conditions, sizes as determined by the three analysis techniques (TEM, AFM and DLS), and the transverse to longitudinal nuclear relaxivity ratio $r_2/r_1$ at 1.34 T for the three selected samples **MNP-6.6**, **MNP-5.3** and **MNP-4.0**, all obtained in diluted conditions (15.6 mM). In parenthesis half of the full width at half maximum ($\sigma_D$) are also reported.

| Sample | Reaction Temp. (°C) | Growth time (min) | Core diameter, TEM (nm) | Core-shell diameter, AFM (nm) | Hydrodynamic diameter, DLS (nm) | $r_2/r_1$ @1.34 T |
|---|---|---|---|---|---|---|
| **MNP-6.6** | RT | 5 | 6.6(2.0) | 8.6 (1) | 16 (6) | 3.3 |
| **MNP-5.3** | 0 | 5 | 5.3 (1.2) | 7.5 (0.8) | 10 (3) | 2.9 |
| **MNP-4.0** | 0 | 1 | 4.0 (0.8) | 6.5 (1.1) | 5.7 (5) | 1.8 |

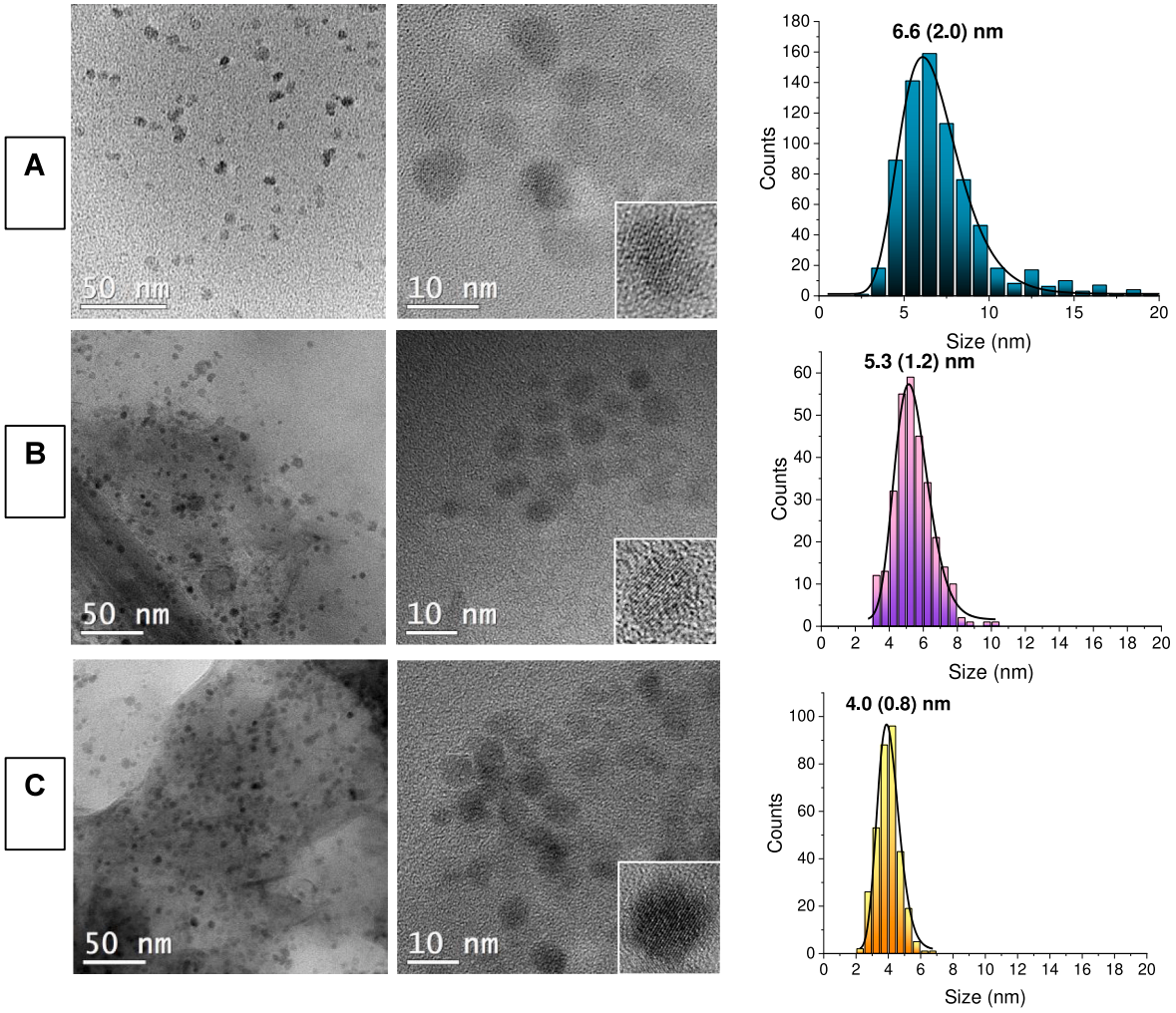


**Fig. 3.** TEM and HRTEM images of samples **MNP-6.6** (panel A), **MNP-5.3** (Panel B), and **MNP-4.0** (Panel C) and relative size distributions all fitted with a lognormal function. The insets magnify one single particle to highlight the lattice fringes. The values reported on the top of the curves are the median values (in parenthesis there are the standard deviation values).

magnetite into maghemite at room temperature.

Upon complete removal of TMAOH, the colloidal stability of the sample decreased markedly, thus causing precipitation of the colloids after a few days. Hence, we investigated through ζ-potential measurements the variation of the surface charge as a function of pH (Fig. 1b). The isoelectric point of MNPs synthesized without the addition of citrate was equal to 5.7, i.e. shifted to more acidic values compared to MNPs synthesized by using either NaOH (iep = 6.85) or $NH_3$ (iep = 7.0), as reported in Fig. S3. The observed shift of the iep has been attributed to the formation of an effective double layer at the surface of the MNPs, with a high amount of negative charges ($OH^-$) and a smaller number of positive charges ($TMA^+$), located at the outer Helmholtz plane at neutral pH. The bulkier and more apolar $TMA^+$ cations with respect to $Na^+$ and $NH_4^+$ are thought to be at the origin of the very stable double layer surrounding the MNPs. The addition of citric acid during synthesis, on the other hand, shifts the isoelectric point to much more acidic values, supporting the adsorption of citrate onto the particle surface. After purification, the isoelectric point remains unchanged, indicating that citrate is still adsorbed on the surface, although to a lesser extent, as evidenced by the less negative zeta potential values. Regardless of pH, the zeta potential values after purification are indicative of colloidal instability.

To promote dispersion stability over time additional citrate was introduced in the purified MNP suspensions until a pH of 7.4 was reached. The so-prepared MNP@citrate resulted stable for several weeks in colloidal suspension even when stored at room temperature (Fig. 1c). Moreover, a preliminary stability test of MNP@citrate was carried out in phosphate buffer solution (PBS), which showed that after 24 h the hydrodynamic diameter was unchanged (Fig. S4), supporting a good stability in moderate ionic strength media. The addition of extra citrate is appreciable in ATR-FTIR spectra (Fig. S5) as a shift in the asymmetric and symmetric stretching of the carboxylate group to 1575 and 1394 $cm^{-1}$ ($\Delta\nu$ = 181 $cm^{-1}$), respectively, reaching values similar to that of trisodium citrate (1591 and 1395 $cm^{-1}$, $\Delta\nu$ = 196 $cm^{-1}$). However, it should be noted that the peak of the asymmetric stretching clearly shows a shoulder at longer wavenumbers. It has been previously reported, based on ATR-FTIR evidence, that citrate possibly forms monodentate/bidentate inner-sphere and outer-sphere complexes with Fe oxide surfaces [43], which could be compatible with the present findings. It should be noted that cytotoxicity and immunofluorescence analyses (see Section 3.4) were carried out on purified samples upon addition of additional citrate.

### 3.2. Role of the synthetic parameters on particle size

We sought to elucidate the role of each parameter on the particle size, namely the amount of TMAOH relative to the iron concentration, the reaction temperature, the overall concentration of the iron

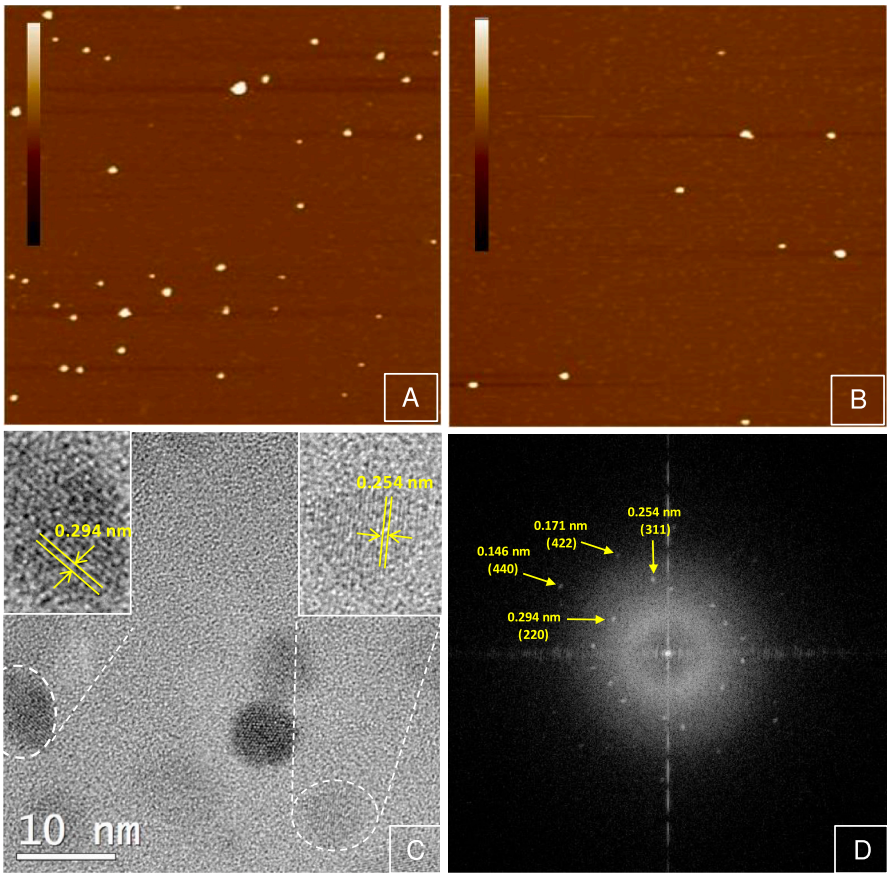


**Fig. 4.** (A, B) AFM topography images of the **MNP-6.6** (A) and **MNP-5.3** (B) samples. Single MNPs as well as MNP small clusters are visualized on a mica support. Scan area: 1 × 1 μm$^2$. Vertical false-colour scale bar: 15 nm. (C, D) HRTEM analysis of **MNP-6.6**: HRTEM image (C) and corresponding fast Fourier transform (FFT) image (D). Inset magnified images of two nanoparticles highlighting two different interplanar distances.

precursors, and the growth time.

### 3.2.1. *Effect of the TMAOH amount*

The TMAOH-to-Fe(III) molar ratio was varied in successive preparations while keeping other parameters constant (RT, 156 mM $Fe^{3+}$, 5 min of growth time), and the results were compared by measuring the hydrodynamic diameter of the nanoparticles using DLS. Table 1 reports the hydrodynamic diameters by intensities of all the populations present in each sample before dialysis. The measurements were repeated also after dialysis showing comparable results (data not shown). While in all samples two populations are always visible in the size distribution by intensities, it is worth noting that the population with the larger size can be attributed to a very small number of aggregates, as clearly shown by the size distribution by numbers, which, on the contrary, always shows only the smaller population. DLS data show that when an excess of TMAOH relative to the stoichiometric ratio (entries 1 and 2 of Table 1) was used, the nanoparticles exhibited a mean hydrodynamic diameter of ca 30-40 nm.

An even higher excess of base (TMAOH-to-Fe(III) > 9) caused the precipitation of the iron oxide nanoparticles during the synthesis. When the TMAOH-to-Fe(III) molar ratio was reduced to 4.8, slightly exceeding the stoichiometric amount, a significant decrease of the average hydrodynamic diameter was observed (entry 3 of Table 1). However, when an approximately stoichiometric amount of TMAOH was used (entry 4 of Table 1), samples appeared poorly reproducible. Thus, it was concluded that, with other parameters remaining unchanged, a reduction in the TMAOH amount led to a decrease in mean nanoparticle diameter. A moderate excess of the stabilizing/peptizing agent ([TMAOH]/[$Fe^{3+}$] = 4.8 versus the stoichiometric ratio of 4) is however required to prevent nanoparticle aggregation before the citric acid exchange.

### 3.2.2. *Initial concentration of iron ions and growth time*

Several syntheses were conducted by varying the initial concentration of Fe(III) ions (156 mM or 15.6 mM in the final volume of 8.0 mL). The stock Fe(III) solution was consistent across experiments, but the volume added at the beginning of each reaction was adjusted (2.5 mL or 250 μL). The total volume of the reaction mixture and reagent ratios were kept constant, with a total volume of 8 mL and molar ratios [TMAOH]/[$Fe^{3+}$] = 4.8 and [$Fe^{3+}$]/[citric acid] = 0.78. Under these conditions, multiple synthesis repetitions with [$Fe^{3+}$]$_0$ set to 156 mM yielded a mean hydrodynamic diameter of 15(2) nm ($\sigma_D$ = 6 nm). When the growth time was set to 5 min, reducing the Fe(III) concentration had no significant effect on the primary peak size (15(3) nm, $\sigma_D$ = 7 nm). However, when the growth time was shortened to 1 min at high concentration, the DLS profile showed a main population significantly larger (24(1) nm, $\sigma_D$ = 12 nm) than that observed under the same concentration conditions but with a longer growth time (5 min). This suggests that under these conditions ([$Fe^{3+}$] = 156 mM, 1 min growth), rapid nucleation kinetics leads to the formation of polydisperse aggregates that do not fully reorganize into a smaller, more monodisperse population over such a short 1 min growth period. Reducing the initial Fe(III) concentration by one order of magnitude led, after 1 min growth, to a smaller mean hydrodynamic diameter (12(1) nm) with a narrower size distribution ($\sigma_D$ = 5 nm). Thus, at room temperature, optimal conditions for minimizing particle size and polydispersity were achieved by lowering the initial Fe(III) concentration ([$Fe^{3+}$]$_0$ = 15.6 mM) and adopting a 1-min growth time. All data are presented in Table 2 and Fig. S6.

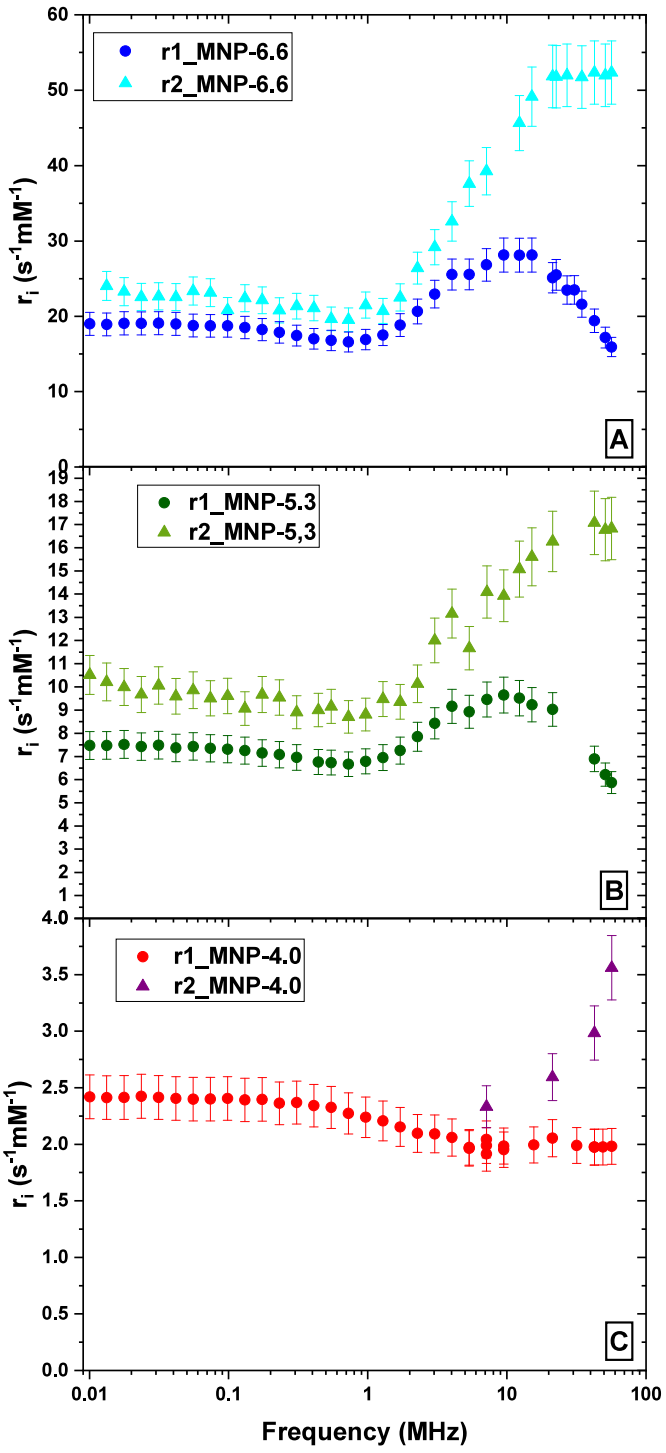


**Fig. 5.** Longitudinal ($r_1$) and transverse ($r_2$) relaxivity $^1$H-NMRD profiles of **MNP-6.6** (panel A), **MNP-5.3** (panel B) and **MNP-4.0** (panel C).

### 3.2.3. Reaction temperature

Typically, the coprecipitation synthesis of iron oxide nanoparticles is conducted at room temperature or moderate temperatures (<100 °C) to improve nanoparticle crystallinity. In this study, we investigated the effect of reaction temperature on nanoparticle growth kinetics first of all by means of DLS, hence following the variation of the hydrodynamic diameter (Fig. 2). We found that lowering the reaction temperature, while keeping other parameters constant, led to a decrease in the size of the magnetite nanoparticles. Tests conducted at 0 °C consistently produced smaller nanoparticles for both the tested concentrations (Table 2). Additional tests at 60 °C produced samples with highly polydisperse populations, as determined by dynamic light scattering (data not shown), which resulted in rapid colloidal instability.

## 3.3. Role of particle size on nuclear relaxometric properties

Following the comprehensive study in which each experimental parameter was individually varied while keeping the others constant, we identified the optimal combination of conditions that enabled us to obtain three MNP samples, named **MNP-6.6**, **MNP-5.3** and **MNP-4.0**, with progressively smaller hydrodynamic diameters to be studied from the point of view of the magnetic resonance properties. Their characteristics are summarized in Table 3 and described in the next paragraphs.

### 3.3.1. Morphological properties

The TEM micrographs were acquired on all three selected samples (Fig. 3, left column), displaying MNP with roundish contours that appeared largely non-aggregated, indicating the ability of citrate to keep the colloidal solution stable by preventing premature aggregation. TEM images are consistent with the DLS data (see Table 3): as the core diameter measured by TEM decreases, the hydrodynamic diameter decreases accordingly, while the size distribution progressively narrows (Fig. 3, right column).

Moreover, AFM was also used to assess the overall size of the MNPs, which includes both the magnetic core and the surrounding organic coating. Furthermore, AFM allowed for the differentiation between MNP agglomerates and individual MNPs. As an example, two AFM topography images of the studied MNPs have been reported in Fig. 4 (panels A and B) and Fig. S7, where both single MNPs and small MNP clusters are clearly visible on the mica support.

The quantitative analysis of AFM topography images allowed to measure the single MNP size; experimental data showed an average diameter of 8.6 ± 1.0, 7.5 ± 0.8, and 6.5 ± 1.1 nm for **MNP-6.6**, **MNP-5.3**, and **MNP-4.0** samples, respectively (see Table 3). MNPs size measurements were performed on 25 single MNPs for **MNP-6-6** and **MNP-5.3** samples and 10 single MNPs for **MNP-4.0** sample due to its higher dilution, as visualized in several AFM topography images collected in different areas. As expected because of the MNPs coating, the average diameter measured by AFM images was larger than that estimated from the TEM data (see Table 3). The thickness of the MNP coating, estimated from the difference in diameter values obtained by the two techniques, was approximately of the order of 1 nm for all the studied MNPs [44,45], suggesting a multilayer citrate coating.

In the HRTEM images, reported in the central column of Fig. 3, the lattice fringes are clearly visible, indicating that the produced MNPs have a good degree of crystallinity. The analysis of both diffraction fringes and Fast Fourier Transform (FFT) patterns of the fringes themselves (Fig. 4c–d and Fig. S8–S9) reveals, for all samples, the presence of crystallographic planes with d = 0.29, 0.25, 0.17 and 0.15 nm, which are compatible with (220), (311), (422) and (440) planes of magnetite (ICDD 19-629) and/or maghemite (ICDD 39-1346).

### 3.3.2. Nuclear Magnetic Relaxation Dispersion (NMRD)

The spin dynamics of MNPs at room temperature was probed indirectly by means of $^1$H NMR relaxometry as a function of proton resonance frequency (Larmor frequency). The longitudinal ($T_1$) and the transverse ($T_2$) nuclear relaxation times enable study of the local electron spin dynamics and evaluation of the MRI contrast efficiency of MNPs through calculation of the nuclear relaxivity $r_i$ (see Equation (2) in 2.3 Instruments and Methods). Indeed, $r_i$ quantify the shortening of $T_1$ and $T_2$ times in the presence of magnetic centres compared to the case of dispersant only, i.e., the increased capacity of image contrast [17]. Therefore, we studied the longitudinal and transverse relaxivity ($r_1$ and $r_2$, respectively) as a function of Larmor frequency, obtaining for each MNP sample the so-called Nuclear Magnetic Relaxation Dispersion

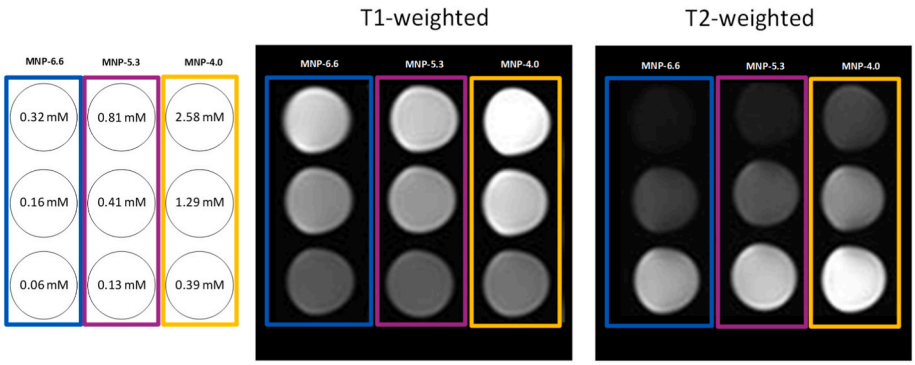


**Fig. 6.** Sample concentrations and displacement scheme (left) for the MRI acquisitions at 3 T: $T_1$-weighted image (centre) and $T_2$-weighted image (right). The imaged samples were **MNP-6.6** (blue), **MNP-5.3** (purple), and **MNP-4.0** (yellow).

**Table 4**
Estimation of relaxivities of the MNP samples at 3 T. Standard deviations as obtained from error propagation are reported in brackets.

| Sample | $r_1$ ($mM^{-1}$ $s^{-1}$) | $r_2$ ($mM^{-1}$ $s^{-1}$) | $r_2/r_1$ @ 3 T |
|---|---|---|---|
| **MNP-6.6** | 5.6 (1.0) | 47.7 (4.9) | 8.5 |
| **MNP-5.3** | 2.4 (0.5) | 16.4 (1.1) | 6.7 |
| **MNP-4.0** | 0.9 (0.2) | 3.2 (0.5) | 3.7 |

**Table 5**
Estimation of relaxation times of the samples at 3 T. Standard deviations as obtained from error propagation are reported in brackets.

| Sample | Concentration (mM) | $T_1$ (ms) | $T_2$ (ms) |
|---|---|---|---|
| **MNP-6.6** | 0.323 | 467 (69) | 63 (6) |
| | 0.161 | 810 (103) | 122 (12) |
| | 0.056 | 1546 (131) | 316 (30) |
| **MNP-5.3** | 0.811 | 434 (70) | 73 (5) |
| | 0.406 | 758 (107) | 140 (9) |
| | 0.131 | 1535 (142) | 378 (23) |
| **MNP-4.0** | 2.584 | 387 (79) | 114 (16) |
| | 1.291 | 687 (123) | 216 (31) |
| | 0.387 | 1492 (175) | 576 (74) |

(NMRD) profile.

Fig. 5 reports $r_1$ and $r_2$ of the three selected samples. As expected [46, 47], lowering the size of the magnetic core of MNPs the values of both relaxivities diminish, confirming the strong dependence of nuclear relaxation properties on the size of MNPs. At the same time, the presence of a $r_1$ maximum at $\nu \approx 10$ MHz in the NMRD profiles for **MNP-6.6** and **MNP-5.3** reflects the typical behaviour of superparamagnetic nanoparticle with diameter $< 20$ nm [48–51], whereas in the case of **MNP-4.0** a small hint of the maximum is present in the range $20 < \nu < 30$ MHz. An indication about the estimate of the MNP magnetic anisotropy can be obtained looking at the "low field dispersion in $r_1$ curve," i.e., the slight dip just after the low frequency plateau. In our case, the dispersion feature becomes less evident passing from **MNP-6.6** to **MNP-4.0**. Considering the $r_i$ values, the evolution of the maximum and the attitude in the low field region of NMRD profiles, MNPs showed a transition from a $T_2$ type relaxing systems (**MNP-6.6** and **MNP-5.3**) to a $T_1$ type one (**MNP-4.0**), as also suggested by the $r_2/r_1$ values at $\nu = 57$ MHz (1.34 T) reported in Table 3.

Other potential effects such as the presence of free citrate molecules can be considered negligible in affecting the differences among the samples. As a matter of fact, the relaxation is described by four possible correlation times: the Néel relaxation time ($\tau_N$) that describes the fluctuation of the electronic magnetic spin of MNPs, the Brownian time ($\tau_B$) and the diffusion time ($\tau_D$), both related to the motion of MNPs, and, wherever present, the so called chemical exchange time ($\tau_{ex}$), related to the exchange process between a water molecule coordinated to the MNP surface and a water molecule of the medium [46]. The presence of free citrate not affecting substantially the viscosity of the medium could not

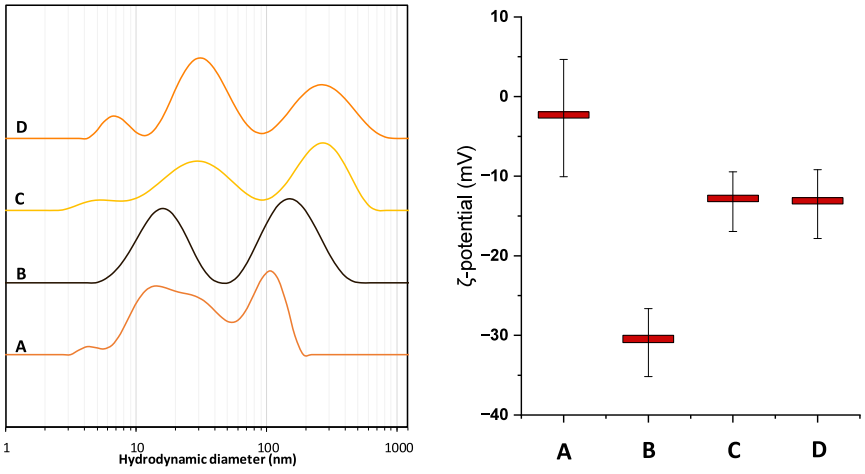


**Fig. 7.** Comparison of DLS size distribution by intensity (Panel A) and relative ζ-potential values (Panel B) for proteins of culture medium and MNP in different environments: culture medium composed by DMEM diluted 1:10 with water + fetal bovine serum 10% + penicillin and streptomycin (red trace, A); purified **MNP-6.6** in milliQ water (dark brown trace, B); purified **MNP-6.6** in culture medium at t = 0h (yellow trace, C); purified **MNP-6.6** in culture medium at t = 36h (orange trace, D). All media were modified with $KNO_3$ (0.01 M).

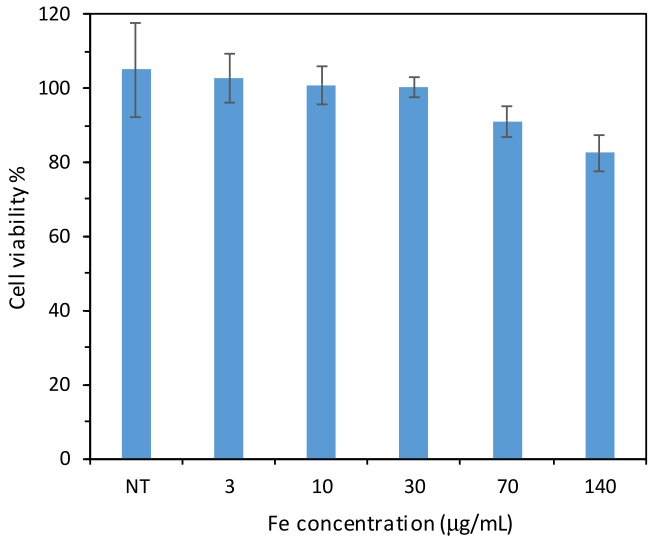


**Fig. 8.** Effect of increasing concentrations of MNPs on HEK cell viability after 72 h of treatment. To the non-treated (NT) cells the same amount of citrate solution 0.01 M without MNPs was added. Each result represents the average value of three different experiments performed in quadruplicate. Cell viability is expressed as percentage compared to untreated cells ± SD.

change $\tau_B$ and $\tau_D$ and for sure it is not able to influence $\tau_N$. The only correlation time that in principle could be modified by the free citrate is the chemical exchange time, but in the same manner for our samples considering the identical preparation for all of them. However, it must be said that the contribution of $\tau_{ex}$ to the nuclear relaxation in MNPs samples is small in comparison to the other correlation times (in particular $\tau_D$ that is the predominant one) and it is important above all for molecular contrast agent systems, namely Gd-based molecules. We can conclude that, if the free citrate effect exists, it should affect all our samples in the same manner, because really small changes could be expected on absolute relaxivity values and no relative difference must exist between their values.

### 3.3.3. Magnetic resonance imaging (MRI)

$T_1$-and $T_2$-weighted spin-echo images, acquired as reported in detail in Section 2.3, of 1 mL MNP aqueous solutions are shown in Fig. 6: the used concentrations were chosen to reach $T_1$ values of ca 1500, 500, and 250 ms for each sample, based on extrapolations from lower field NMRD profiles. As expected from the NMRD results, increasingly higher concentrations are needed to achieve the desired $T_1$ values with decreasing diameters of MNPs.

Differences in signal intensities (S) can be explained in terms of the ratio between transverse and longitudinal relaxivities (see Table 4), provided that the expression for the signal at a certain concentration $C$ in spin-echo MRI images is:

$$S(C) \propto \exp\left(-\frac{T_E}{T_2}\right)\left(1-2\exp\left(-\frac{T_R}{T_1}\right)\right) \quad \text{(eq. 3)}$$

where $T_E$ and $T_R$ are the Echo Time and the Repetition Time, respectively.

Given eq. (3), some considerations can be made that lead to a plausible estimation of both relaxivities and relaxation times of the samples at 3 T. Considering the $T_2$-weighted image where, with the chosen acquisition parameters, the condition $T_R \gg T_1$ can be assumed satisfied, the transverse relaxivity $r_2$ can be obtained by the ratio between the signals $S_a$ and $S_b$ from the same MNPs at different concentrations $C_a$ and $C_b$ using the following expression:

$$r_2 = \frac{-\ln\left(\frac{S_a}{S_b}\right)}{T_E\,(C_a - C_b)} \quad \text{(eq. 4)}$$

An estimation of $r_1$ can be then performed by fitting the signal of the samples at different concentrations in $T_1$-weighted images using:

$$S(C) = S_0 \exp\left(-T_E\left(\frac{1}{T_{2w}} + r_2 C\right)\right)\left(1-\exp\left(-T_R\left(\frac{1}{T_{1w}} + r_1 C\right)\right)\right) \quad \text{(eq. 5)}$$

with $S_0$ and $r_1$ as adjustable parameters ($S_0$ is the intrinsic signal intensity; $T_{1w}$ and $T_{2w}$ represent the relaxation times of the water). The fitting plots are reported in the Supplementary Material (Fig. S10 and S11).

Table 4 and Table 5 show the results of the MRI images analysis for the estimation of relaxivities and relaxation times of the samples at 3 T.

In the $T_1$-weighted image, the brightest spot is the vial containing **MNP-4.0** confirming the ability of these nanoparticles to act as positive agents in MRI, having the lowest $r_2/r_1$ ratio. Conversely, **MNP-6.6** and **MNP-5.3** even though remain prevailingly $T_2$-relaxing agents, show an appreciable $T_1$ relaxing ability, making them suitable as dual MRI contrast agents.

### 3.4. Cell uptake and cytotoxicity

Before performing the cell viability assays, we investigated the behaviour of MNPs in the culture medium by DLS as well as ζ-potential measurements. The hydrodynamic size distribution of **MNP-6.6** suspended in DMEM supplemented with 0.01 M $KNO_3$ and fetal bovine serum was determined (Fig. 7). This medium was select as it was used for in vitro assays; moreover, it is widely regarded as the gold standard for the determination of colloidal stability in physiological conditions, as the presence of proteins like BSA allows the possible formation of a protein corona, thus enabling the determination of hydrodynamic size and ζ-potential values indicative of the actual physiological conditions. Prior to the measurements, the samples were diluted 1:10 with Milli-Q water to meet instrumental requirements. The resulting **MNP-6.6** suspensions remained unchanged over time (traces C, t = 0, and D, t = 36 h), showing three peaks: one at 5-6 nm attributed to medium proteins, one at 30 nm corresponding to MNPs, and a third at 270 nm due to a small fraction of aggregates. Compared to the **MNP-6.6** in pure water, the main MNP peak shifted from 16 to 30 nm, suggesting the formation of a protein corona on the MNP surface. The protein corona may stabilize the MNPs in a medium with high ionic strength, whereas in pure water the same conditions would destabilize the MNPs, causing aggregation and precipitation. In parallel, the ζ -potential decreased from −30 mV for MNP in pure water to −13 mV in culture medium, corroborating the idea of the formation of a protein corona. It is noteworthy that surface functionalization plays a key role in determining the hemocompatibility of magnetic nanoparticles. Negatively charged coatings, such as citrate, generally reduce hemolytic activity [52], and the formation of a protein corona further decreases hemolysis [53].

Biocompatibility studies were performed to obtain experimental information on the suitability of MNPs for biomedical applications. HEK cells (Human Embryonic Kidney 293 cells), widely used in various scientific and pharmaceutical applications, were incubated with increasing concentrations of MNPs ranking from 3 to 140 μg/mL and cell viability was measured after 72 h. To account for the possible cytotoxic effect of excess-citrate present in the MNP suspension (see the Experimental section for details), HEK cells were also treated with citrate at the same concentration found in the supplemented MNP suspensions (referred to as NT in the graph in Fig. 8). No cytotoxic effects were observed at the employed concentration, confirming that citrate did not affect cell viability. MNPs were well tolerated even at the highest concentrations, which were associated with viability >80% (Fig. 8).

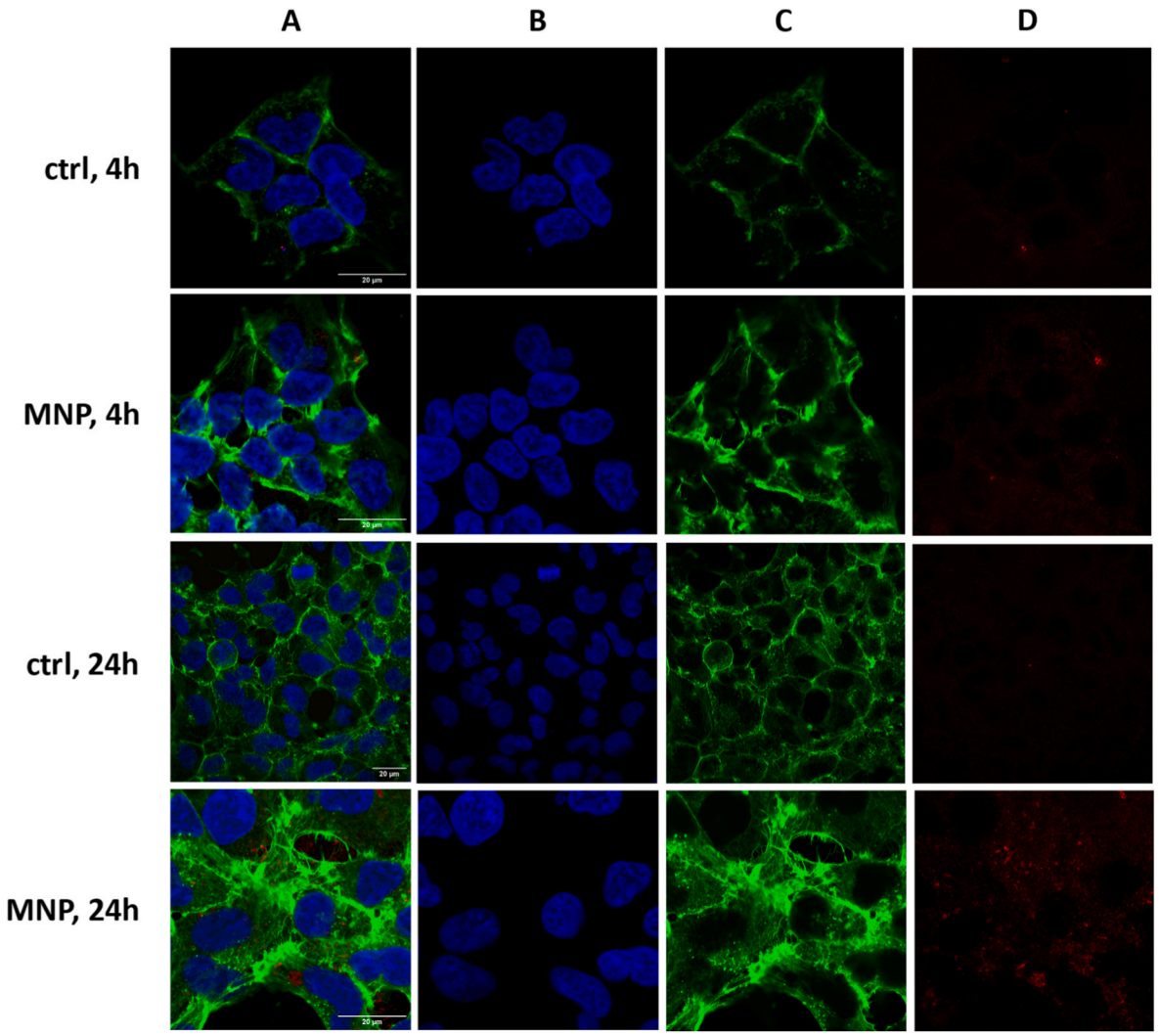


**Fig. 9.** Confocal microscopy images of HEK cells treated with **MNP-6.6** both 4 and 24 h compared A) Superposition of the three channels; B) Hoesch fluorescence (blue) visualizing the nuclei; C) Phalloidin fluorescence (green) visualizing the cytoskeleton; D) Reflected light (red) localizing the MNPs.

Then, the ability of MNPs to enter cells was tested and the kinetic uptake was studied by incubating HEK cells with MNPs for 4 and 24 h. Confocal images revealed a consistent accumulation of MNPs inside the cells at longer time point, while a very faint signal was detectable at 4 h (Fig. 9). The assay was carried out after the nuclei and cytoskeleton were stained with Hoechst and phalloidin, respectively, revealing that MNPs mainly accumulated at the cytoplasmic level.

Our data show that MNPs can be internalized by cells and are well tolerated, indicating that they can represent an effective system in the field of clinical diagnosis and biomedical research.

## 4. Conclusions

Iron oxide nanoparticles are important for a wide range of applications for which size control is often essential; however, this generally requires syntheses under harsh conditions and a workup to make them water-dispersible and biocompatible. Among these applications, particularly relevant is their use as contrast agents in MRI, for which obtaining ultrasmall particles ($d < 5$ nm) is crucial to achieve positive contrast. In this work, we developed a robust and simple coprecipitation synthesis that led to the preparation of spherical ultrasmall MNPs with well controlled size distribution and stable colloidal dispersion in water, also in the presence of high magnetic field as in MRI measurements. The MNP size could be easily tuned by adjusting the precursor concentration, the reaction temperature, and the growth time.

The innovative use of TMAOH as base – and not simply as a peptizing agent – played a key role for the obtainment of ultrasmall non-aggregated magnetite-based nanoparticles. Indeed, unlike other bases such as NaOH or $NH_3$, TMAOH does not promote MNP precipitation but, instead, fundamentally contributes to the immediate formation of a stable colloidal suspension.

After the removal of all the TMAOH, the MNPs stabilized only by citrate remained suspended over several months and remained stable even under applied magnetic fields up to 3 T.

The MNPs showed dual $T_1$ and $T_2$ relaxing properties, with the expected increase in $T_1$ relaxing abilities as the MNP size decreased, as also confirmed by in vitro MRI results.

The strong stability of MNPs in the culture medium, as assessed by DLS and ζ-potential measurements, along with the observed increase in hydrodynamic size and reduction in ζ-potential in supplemented DMEM, suggest the formation of a protein corona on the MNP surface. This protein layer is likely responsible for enhancing nanoparticle stability under high ionic strength conditions, such as those found in physiological environments. Biocompatibility studies conducted on HEK cells showed that the MNPs are well tolerated even at high concentrations, with cell viability remaining above 80% after 72 h. Cellular uptake experiments revealed a time-dependent internalization, with preferential accumulation in the cytoplasm after 24 h.

Overall, these results indicate that these MNPs are biocompatible and capable of entering cells, supporting their further evaluation as MRI contrast agents.

## CRediT authorship contribution statement

**Daniela Meroni:** Writing – original draft, Supervision, Resources, Project administration, Methodology, Investigation, Conceptualization. **Davide Cicolari:** Writing – review & editing, Investigation, Formal analysis. **Giorgia Colciago:** Visualization, Validation, Investigation. **Tommaso Taroni:** Visualization, Validation, Investigation. **Laura Rossi:** Writing – review & editing, Resources, Methodology. **Marco Maria Jacopo Felisi:** Resources. **Paola Enrica Colombo:** Resources. **Francesco Orsini:** Writing – review & editing, Resources, Methodology, Investigation. **Riccardo Vago:** Writing – review & editing, Resources, Methodology. **Daniela Maggioni:** Writing – original draft, Supervision, Resources, Project administration, Methodology, Conceptualization. **Paolo Arosio:** Writing – review & editing, Validation, Resources, Methodology, Investigation.

## Declaration of competing interests

The authors declare that they have no known competing financial interests or personal relationships that could have appeared to influence the work reported in this paper.

## Acknowledgement

This work was supported by the Università degli Studi di Milano (project PSR2025_DIP_005_PI_GDICA). All the authors thank Dr. Miriam Ascagni of NOLIMITS and Dr. Nicola Rotiroti of COSPECT, for the analyses carried out at these two advanced imaging facilities established by the Università degli Studi di Milano.

## Appendix A. Supplementary data

Supplementary data to this article can be found online at https://doi.org/10.1016/j.mtchem.2026.104002.

## Data availability

Data will be made available on request.

## References

[1] P. Arosio, D. Cicolari, A. Manfredi, F. Orsini, A. Lascialfari, E. Ranucci, P. Ferruti, D. Maggioni, Nanosized T1 MRI contrast agent based on a polyamidoamine as multidentate Gd ligand, Molecules 27 (2022) 174–196, https://doi.org/10.3390/molecules27010174.
[2] J. Ramalho, R.C. Semelka, M. Ramalho, R.H. Nunes, M. AlObaidy, M. Castillo, Gadolinium-based contrast agent accumulation and toxicity: an update, Am. J. Neuroradiol. 37 (2016) 1192–1198, https://doi.org/10.3174/ajnr.A4615.
[3] J.L. Domingo, R.C. Semelka, Gadolinium toxicity: mechanisms, clinical manifestations, and nanoparticle role, Arch. Toxicol. 99 (2025) 3897–3916, https://doi.org/10.1007/s00204-025-04124-x.
[4] M.E. Lorkowski, P.U. Atukorale, K.B. Ghaghada, E. Karathanasis, Stimuli-responsive iron oxide nanotheranostics: a versatile and powerful approach for cancer therapy, Adv. Healthc. Mater. 10 (2021), https://doi.org/10.1002/adhm.202001044.
[5] S. Surasinghe, I. Liatsou, Z. Nováková, C. Bařinka, D. Artemov, S. Hapuarachchige, Optical and MRI-guided theranostic application of ultrasmall superparamagnetic iron oxide nanodrug conjugate for PSMA-positive prostate cancer therapy, ACS Appl. Mater. Interfaces 17 (2025) 11611–11623, https://doi.org/10.1021/acsami.4c16009.
[6] S. Leon-Chaviano, M. Kiseleva, P. Legros, S. Collin, T. Lescot, C. Henoumont, Y. Gossuin, S. Laurent, D. Mayrand, J. Fradette, A. Bégin-Drolet, J. Ruel, M. Fortin, A nanoparticle ink allowing the high precision visualization of tissue engineered scaffolds by MRI, Small 19 (2023), https://doi.org/10.1002/smll.202206644.
[7] X. Feng, Y. Xue, S. Gonca, K. Ji, M. Zhang, F.R. García-García, Q. Li, Y. Huang, K. V. Kamenev, X. Chen, Ultrasmall superparamagnetic iron oxide nanoparticles for enhanced tumor penetration, J. Mater. Chem. B 11 (2023) 3422–3433, https://doi.org/10.1039/D2TB02630A.
[8] X. Wu, H. Choe, J. Strayer, J. Gómez-Pastora, M. Zborowski, B. Wyslouzil, J. Chalmers, Numerical modeling and in situ small angle X-ray scattering characterization of ultra-small SPION magnetophoresis in a high field and gradient separator, Nanoscale 16 (2024) 7041–7057, https://doi.org/10.1039/D3NR05589B.
[9] Y. Zhang, X. Wang, C. Chu, Z. Zhou, B. Chen, X. Pang, G. Lin, H. Lin, Y. Guo, E. Ren, P. Lv, Y. Shi, Q. Zheng, X. Yan, X. Chen, G. Liu, Genetically engineered magnetic nanocages for cancer magneto-catalytic theranostics, Nat. Commun. 11 (2020) 5421, https://doi.org/10.1038/s41467-020-19061-9.
[10] A. Hervault, N.T.K. Thanh, Magnetic nanoparticle-based therapeutic agents for thermo-chemotherapy treatment of cancer, Nanoscale 6 (2014) 11553–11573, https://doi.org/10.1039/C4NR03482A.
[11] S. Lopez, N. Hallali, Y. Lalatonne, A. Hillion, J.C. Antunes, N. Serhan, P. Clerc, D. Fourmy, L. Motte, J. Carrey, V. Gigoux, Magneto-mechanical destruction of cancer-associated fibroblasts using ultra-small iron oxide nanoparticles and low frequency rotating magnetic fields, Nanoscale Adv. 4 (2022) 421–436, https://doi.org/10.1039/D1NA00474C.
[12] D. Maggioni, P. Arosio, F. Orsini, A.M. Ferretti, T. Orlando, A. Manfredi, E. Ranucci, P. Ferruti, G. D'Alfonso, A. Lascialfari, Superparamagnetic iron oxide nanoparticles stabilized by a poly(amidoamine)-rhenium complex as potential theranostic probe, Dalt. Trans. 43 (2014) 1172–1183, https://doi.org/10.1039/C3DT52377B.
[13] H.E. Daldrup-Link, Ten things you might not know about iron oxide nanoparticles, Radiology 284 (2017) 616–629, https://doi.org/10.1148/radiol.2017162759.
[14] S. Laurent, J.-L. Bridot, L. Vander Elst, R.N. Muller, Magnetic iron oxide nanoparticles for biomedical applications, Future Med. Chem. 2 (2010) 427–449, https://doi.org/10.4155/fmc.09.164.
[15] A. Avasthi, C. Caro, E. Pozo-Torres, M.P. Leal, M.L. García-Martín, Magnetic Nanoparticles as MRI Contrast Agents, 2020, pp. 49–91, https://doi.org/10.1007/978-3-030-55502-3_3.
[16] M. Basini, A. Guerrini, M. Cobianchi, F. Orsini, D. Bettega, M. Avolio, C. Innocenti, C. Sangregorio, A. Lascialfari, P. Arosio, Tailoring the magnetic core of organic-coated iron oxides nanoparticles to influence their contrast efficiency for magnetic resonance imaging, J. Alloys Compd. 770 (2019) 58–66, https://doi.org/10.1016/j.jallcom.2018.08.120.
[17] C. Burtea, S. Laurent, L. Vander Elst, R.N. Muller, Contrast agents, Magnetic Resonance (2008) 135–165, https://doi.org/10.1007/978-3-540-72718-7_7.
[18] H. Wei, O.T. Bruns, M.G. Kaul, E.C. Hansen, M. Barch, A. Wiśniowska, O. Chen, Y. Chen, N. Li, S. Okada, J.M. Cordero, M. Heine, C.T. Farrar, D.M. Montana, G. Adam, H. Ittrich, A. Jasanoff, P. Nielsen, M.G. Bawendi, Exceedingly small iron oxide nanoparticles as positive MRI contrast agents, Proc. Natl. Acad. Sci. 114 (2017) 2325–2330, https://doi.org/10.1073/pnas.1620145114.
[19] M. Jeon, M.V. Halbert, Z.R. Stephen, M. Zhang, Iron oxide nanoparticles as T 1 contrast agents for magnetic resonance imaging: fundamentals, challenges, applications, and prospectives, Adv. Mater. 33 (2021), https://doi.org/10.1002/adma.201906539.
[20] H. Lu, A. Chen, X. Zhang, Z. Wei, R. Cao, Y. Zhu, J. Lu, Z. Wang, L. Tian, A pH-responsive T1-T2 dual-modal MRI contrast agent for cancer imaging, Nat. Commun. 13 (2022) 7948, https://doi.org/10.1038/s41467-022-35655-x.
[21] W. Liu, S.-Y. Yin, Y. Hu, T. Deng, J. Li, Microemulsion-confined assembly of magnetic nanoclusters for pH/H 2 O 2 dual-responsive T 2 –T 1 switchable MRI, ACS Appl. Mater. Interfaces 14 (2022) 2629–2637, https://doi.org/10.1021/acsami.1c22747.
[22] J. Yang, J. Feng, S. Yang, Y. Xu, Z. Shen, Exceedingly small magnetic iron oxide nanoparticles for T 1 -weighted magnetic resonance imaging and imaging-guided therapy of tumors, Small 19 (2023), https://doi.org/10.1002/smll.202302856.
[23] C. Lu, Y. Bao, Z. Fei, Z. Wang, J. Ma, R. Ren, X. Xu, Y. Zhang, Multielement doping engineered iron oxide nanoparticles: enabling the shift from negative to positive MRI contrast for enhanced diagnostic precision, Small 21 (2025), https://doi.org/10.1002/smll.202410414.
[24] M.O. Besenhard, A.P. LaGrow, A. Hodzic, M. Kriechbaum, L. Panariello, G. Bais, K. Loizou, S. Damilos, M. Margarida Cruz, N.T.K. Thanh, A. Gavriilidis, Co-precipitation synthesis of stable iron oxide nanoparticles with NaOH: new insights and continuous production via flow chemistry, Chem. Eng. J. 399 (2020) 125740, https://doi.org/10.1016/j.cej.2020.125740.
[25] G. Wang, X. Zhang, A. Skallberg, Y. Liu, Z. Hu, X. Mei, K. Uvdal, One-step synthesis of water-dispersible ultra-small Fe3O4 nanoparticles as contrast agents for T1 and T2 magnetic resonance imaging, Nanoscale 6 (2014) 2953, https://doi.org/10.1039/c3nr05550g.
[26] D. Zhang, J. Zhang, X. Bian, P. Zhang, W. Wu, X. Zuo, Iron oxide nanoparticle-based T1 contrast agents for magnetic resonance imaging: a review, Nanomaterials 15 (2024) 33, https://doi.org/10.3390/nano15010033.
[27] B. Chen, Z. Guo, C. Guo, Y. Mao, Z. Qin, D. Ye, F. Zang, Z. Lou, Z. Zhang, M. Li, Y. Liu, M. Ji, J. Sun, N. Gu, Moderate cooling coprecipitation for extremely small iron oxide as a pH dependent T 1 -MRI contrast agent, Nanoscale 12 (2020) 5521–5532, https://doi.org/10.1039/C9NR10397J.
[28] F. Brero, P. Arosio, M. Albino, D. Cicolari, M. Porru, M. Basini, M. Mariani, C. Innocenti, C. Sangregorio, F. Orsini, A. Lascialfari, 1H-NMR relaxation of ferrite core-shell nanoparticles: evaluation of the coating effect, Nanomaterials 13 (2023) 804, https://doi.org/10.3390/nano13050804.
[29] A.E. Harvey, J.J.A. Smart, E.S. Amis, Simultaneous spectrophotometric determination of Iron(II) and total iron with 1,10-Phenanthroline, Anal. Chem. 27 (1955) 26, https://doi.org/10.1021/ac60097a009.
[30] E. Anoardo, G. Galli, G. Ferrante, Fast-field-cycling NMR: applications and instrumentation, Appl. Magn. Reson. 20 (2001) 365–404, https://doi.org/10.1007/BF03162287.

[31] H. Hamza, V. Schifano, G. Colciago, M.A. Ortenzi, A.M. Ferretti, G. Di Carlo, M. V. Dozzi, R. Vago, F. Tessore, D. Maggioni, Halloysite nanotubes as a vector for hydrophobic perfluorinated porphyrin-based photosensitizers for singlet oxygen generation, Nanoscale 17 (2025) 18935–18947, https://doi.org/10.1039/D5NR01078K.
[32] T. Girardet, P. Venturini, H. Martinez, J.-C. Dupin, F. Cleymand, S. Fleutot, Spinel magnetic iron oxide nanoparticles: properties, synthesis and washing methods, Appl. Sci. 12 (2022) 8127, https://doi.org/10.3390/app12168127.
[33] A.P. LaGrow, M.O. Besenhard, A. Hodzic, A. Sergides, L.K. Bogart, A. Gavriilidis, N. T.K. Thanh, Unravelling the growth mechanism of the co-precipitation of iron oxide nanoparticles with the aid of synchrotron X-Ray diffraction in solution, Nanoscale 11 (2019) 6620–6628, https://doi.org/10.1039/C9NR00531E.
[34] K. Mejía-Carmona, M.F. Gustà, P. Guardia, M.C. Spadaro, J. Arbiol, V. Puntes, N. G. Bastús, Size control of highly monodisperse citrate-stabilized magnetite nanoparticles in aqueous media: the role of cerium cations, Chem. Mater. 37 (2025) 7846–7857, https://doi.org/10.1021/acs.chemmater.5c01492.
[35] M.O. Besenhard, L. Panariello, C. Kiefer, A.P. LaGrow, L. Storozhuk, F. Perton, S. Begin, D. Mertz, N.T.K. Thanh, A. Gavriilidis, Small iron oxide nanoparticles as MRI T 1 contrast agent: scalable inexpensive water-based synthesis using a flow reactor, Nanoscale 13 (2021) 8795–8805, https://doi.org/10.1039/D1NR00877C.
[36] Â.L. Andrade, J.D. Fabris, J.D. Ardisson, M.A. Valente, J.M.F. Ferreira, Effect of tetramethylammonium hydroxide on nucleation, surface modification and growth of magnetic nanoparticles, J. Nanomater. 2012 (2012) 1–10, https://doi.org/10.1155/2012/454759.
[37] R. Massart, Preparation of aqueous magnetic liquids in alkaline and acidic media, IEEE Trans. Magn. 17 (1981) 1247–1248, https://doi.org/10.1109/TMAG.1981.1061188.
[38] T. Granath, K. Mandel, P. Löbmann, The significant influence of the pH value on citrate coordination upon modification of superparamagnetic iron oxide nanoparticles, Part. Part. Syst. Charact. 39 (2022), https://doi.org/10.1002/ppsc.202100279.
[39] C. Fosse, L. Mathieu, A.H. Hall, E. Bocchietto, F. Burgher, M. Fischbach, H. I. Maibach, Decontamination of tetramethylammonium hydroxide (TMAH) splashes: promising results with diphoterine ® in vitro, Cutan. Ocul. Toxicol. 29 (2010) 110–115, https://doi.org/10.3109/15569521003661288.
[40] S. Jayakumar, B.B. Lahiri, A. Dasgupta, Preparation, characterization, and application of citrate-functionalized cobalt-doped iron oxide nanoparticles for rhodamine dye and lead ion sequestration, Magnetochemistry 11 (2025) 24, https://doi.org/10.3390/magnetochemistry11040024.
[41] C.C.R. Sutton, G. da Silva, G.V. Franks, Modeling the IR spectra of aqueous metal carboxylate complexes: correlation between bonding geometry and stretching mode wavenumber shifts, Chem. Eur J. 21 (2015) 6801–6805, https://doi.org/10.1002/chem.201406516.
[42] M. Stoia, R. Istratie, C. Păcurariu, Investigation of magnetite nanoparticles stability in air by thermal analysis and FTIR spectroscopy, J. Therm. Anal. Calorim. 125 (2016) 1185–1198, https://doi.org/10.1007/s10973-016-5393-y.
[43] S. Yeasmin, B. Singh, R.S. Kookana, M. Farrell, D.L. Sparks, C.T. Johnston, Influence of mineral characteristics on the retention of low molecular weight organic compounds: a batch sorption–desorption and ATR-FTIR study, J. Colloid Interface Sci. 432 (2014) 246–257, https://doi.org/10.1016/j.jcis.2014.06.036.
[44] S. Monti, G. Barcaro, L. Sementa, V. Carravetta, H. Ågren, Characterization of the adsorption dynamics of trisodium citrate on gold in water solution, RSC Adv. 7 (2017) 49655–49663, https://doi.org/10.1039/C7RA10759E.
[45] J.-W. Park, J.S. Shumaker-Parry, Structural study of citrate layers on gold nanoparticles: role of intermolecular interactions in stabilizing nanoparticles, J. Am. Chem. Soc. 136 (2014) 1907–1921, https://doi.org/10.1021/ja4097384.
[46] P. Arosio, F. Orsini, F. Brero, M. Mariani, C. Innocenti, C. Sangregorio, A. Lascialfari, The effect of size, shape, coating and functionalization on nuclear relaxation properties in iron oxide core–shell nanoparticles: a brief review of the situation, Dalt. Trans. 52 (2023) 3551–3562, https://doi.org/10.1039/D2DT03387A.
[47] L.V. Che Dji, R. Kaddah, T. Girardet, S. Fleutot, S. Bouguet-Bonnet, Effect of the dispersion medium on NMR relaxation properties of superparamagnetic iron oxide nanoparticles between 0.24 mT and 14.1 T, Langmuir 40 (2024) 22089–22097, https://doi.org/10.1021/acs.langmuir.4c02448.
[48] A. Roch, R.N. Muller, P. Gillis, Theory of proton relaxation induced by superparamagnetic particles, J. Chem. Phys. 110 (1999) 5403–5411, https://doi.org/10.1063/1.478435.
[49] M. Lévy, F. Gazeau, C. Wilhelm, S. Neveu, M. Devaud, P. Levitz, Revisiting MRI contrast properties of nanoparticles: beyond the superparamagnetic regime, J. Phys. Chem. C 117 (2013) 15369–15374, https://doi.org/10.1021/jp404199f.
[50] S.H. Koenig, K.E. Kellar, Theory of 1/T 1 and 1/T 2 NMRD profiles of solutions of magnetic nanoparticles, Magn. Reson. Med. 34 (1995) 227–233, https://doi.org/10.1002/mrm.1910340214.
[51] A. Roch, R.N. Muller, P. Gillis, Water relaxation by SPM particles: neglecting the magnetic anisotropy? A caveat, J. Magn. Reson. Imaging. 14 (2001) 94–96, https://doi.org/10.1002/jmri.1157.
[52] S. Malehmir, M.A. Esmaili, M. Khaksary Mahabady, A. Sobhani-Nasab, A. Atapour, M.R. Ganjali, A. Ghasemi, A. Moradi Hasan-Abad, A review: hemocompatibility of magnetic nanoparticles and their regenerative medicine, cancer therapy, drug delivery, and bioimaging applications, Front. Chem. 11 (2023), https://doi.org/10.3389/fchem.2023.1249134.
[53] S. Yedgar, G. Barshtein, A. Gural, Hemolytic activity of nanoparticles as a marker of their hemocompatibility, Micromachines 13 (2022) 2091, https://doi.org/10.3390/mi13122091.